Sideband-Harmonic Instability of Paralleled Inverters with Asynchronous Carriers

Yang, Dongsheng; Wang, Xiongfei; Blaabjerg, Frede

Published in:
I E E E Transactions on Power Electronics

DOI (link to publication from Publisher):
10.1109/TPEL.2017.2731313

Publication date:
2018

Document Version
Accepted author manuscript, peer reviewed version

Citation for published version (APA):
Yang, D., Wang, X., & Blaabjerg, F. (2018). Sideband-Harmonic Instability of Paralleled Inverters with Asynchronous Carriers. *I E E E Transactions on Power Electronics*, *33*(6), 4571-4577 . https://doi.org/10.1109/TPEL.2017.2731313

Sideband Harmonic Instability of Paralleled Inverters with Asynchronous Carriers

Dongsheng Yang, *Member, IEEE*, Xiongfei Wang, *Senior Member, IEEE*, Frede Blaabjerg, *Fellow, IEEE*
doy@et.aau.dk, xwa@et.aau.dk, fbl@et.aau.dk

Abstract—**Paralleled inverters with asynchronous carriers are increasingly emerging into renewable power plants and other power-electronic-based power systems. The sideband harmonics resulting from the pulse width modulation tend to be different from one inverter to another, which may trigger sideband harmonic resonances among the paralleled inverters. To address the sideband harmonic instability, the nonlinearity of the digital pulse width modulator is analyzed first in this paper based on the harmonic balance principle. It is revealed that the dynamic sideband components corresponding to a given small-signal perturbation can be far below the Nyquist frequency, and they may not be effectively attenuated by anti-aliasing filters. A multi-frequency impedance model is then developed for the inverter, which characterizes the dynamic coupling between the perturbed frequency component and the sideband frequency component. The impact of asynchronous carriers on the sideband harmonic instability of paralleled inverters can thus be analyzed, and the frequency and phase sequence of the resulting oscillation components are predicted. Experimental results of two paralleled inverters confirm the effectiveness of the developed model and the stability analysis.**

Index Terms—**Asynchronous carriers, grid-connected inverters, sideband harmonics, multi-frequency model.**

I. INTRODUCTION

OVER the past decade, renewable energy based distributed power generations have been continuously integrated into power grids [1]. Multi-parallel grid-connected inverters are increasingly found in renewable power plants and distribution networks. The dynamic coupling of paralleled inverters through the upstream grid impedance tends to bring in a wide frequency range of resonances, challenging stable operations of modern power systems [2].

Low-frequency resonances are often associated with the power and synchronization control loops of inverters, including the Phase-Locked Loop (PLL), DC-link voltage control and power control. It is reported that the PLL tends to make the inverter behave like a negative resistor at the point of coupling (PCC) [3], [4], which may lead to resonances or unexpected harmonics under the weak grid condition [5]. The stability impact of the DC-link voltage control is investigated in [6], considering the different grid conditions. It is revealed that the PLL and reactive power control loop can introduce a partial positive feedback into the dc-link voltage control in weak grids, which may destabilize the system [7]. Moreover, oscillation phenomena in the time scale of DC-link voltage control may take place among the paralleled inverters, which resembles the rotor dynamics of conventional Synchronous Generators (SGs) [8]. Apart from the low-frequency resonances, the harmonic frequency resonances may also be triggered by the interactions of the wideband control loops, e.g. current control loop, of paralleled inverters. Moreover, the passive components, such as the commonly used *LCL*-filters of inverters, reactive power compensation capacitors and parasitic capacitors of power cables, tend to introduce or magnify the harmonic resonances [9]-[11]. Such phenomena are increasingly reported in renewable power plants, electrical traction system [12]-[13], challenging the grid stability and power quality.

To effectively address the challenges above, the impedance-based approach has been recently developed in [14], [15], which not only provides an intuitive insight of the interactions among the paralleled inverters but also enables to reshape inverter control output impedance for stabilizing the power system [16]-[17]. The impedance model developed for the stability analysis is usually based on the averaged small-signal model, where the sideband harmonics generated by the digital modulator have been neglected by small ripple approximation [18]. However, this is not always true. By employing the high-order filters, such as LCL filter, LLCL filter, LTCL filter, etc., the resonance frequency of filters can be designed to be near or even beyond the Nyquist frequency for a cost-effective design without compromising the quality of the injected grid current [19]-[21]. In this case, the sideband components may impose a significant impact on the dynamics of the inverters. The sideband harmonic resonance may be triggered among the paralleled inverters when their carrier waveforms of modulation are not ideally synchronized. Such high-frequency resonances may induce higher power losses in the passive components which can make them overloaded. But this resonance cannot be characterized by the conventional impedance models. A crossover filter has been used in [22] to characterize the asynchronous-carrier-related resonance. However, this approach merely provides an intuitive explanation on the effect of sideband harmonics. It fails to mathematically reveal the underlying dynamic mechanism. In [23], a multi-frequency impedance matrix has been developed to reveal the sideband harmonic oscillations in dc nano grid. Yet, both the multi-frequency model and the impedance matrix are established at the dc steady-state operating point, which is not readily used for the paralleled inverters, due to the time-varying operating point with the sinusoidal fundamental waveform. In [24], multiple-frequency input admittance is derived to assess the passivity of the inverter above the Nyquist frequency. It only considers the sideband harmonics generated by sampling processes, while neglecting the sideband harmonics generated by the sinusoidal

PWM modulator.

In this paper, a multi-frequency transfer function matrix is proposed for digital sinusoidal PWM modulator based on the harmonic balance principle, where the relationship between the perturbation frequency component and the sideband frequency component is established by injecting a perturbation along a given periodically time varying operation trajectory. Based on the transfer function matrix, a multi-frequency impedance model of the inverter is developed to accurately characterize the output behavior at the PCC including the sideband components. The dynamic impacts of asynchronous carriers on paralleled inverters can thus be mathematically revealed, and consequently, the characteristic of the sideband harmonic instability can be identified. Experimental results from two paralleled inverters confirm the theoretical analysis.

II. ACCURATE MODELING OF THE DIGITAL SINUSOIDAL PWM MODULATOR

Compared with the harmonic spectrum of PWM modulation in DC system, the harmonic spectrum of sinusoidal PWM modulation in AC system is much more complicated when the reference modulating waveform contains both the fundamental and perturbation components. Moreover, when the digital control is employed, the sampling and hold (S&H) procedure also introduces sideband components [24]. Therefore, when the sampling frequency is different from the switching (carrier-) frequency, the output of the digital sinusoidal PWM modulator will contain multiple sideband harmonics. Common practice in modeling the digital sinusoidal PWM modulator is to use Zero-Order Hold (ZOH), which can be expressed by:

$$G_h(s)=\frac{1-e^{-T_s s}}{T_s s} \tag{1}$$

where T_s is the sampling frequency.

However, the ZOH only takes the S&H procedure into consideration, which neglects the inherent nonlinearity of the sinusoidal PWM. As shown in Fig.1, an obvious mismatch can be observed between the output waveform of ZOH and a digital sinusoidal PWM modulator. Hence, such a ZOH model is inadequate to capture the sideband component of the digital sinusoidal PWM modulator.

The harmonics in the output of the digital sinusoidal PWM modulator can be divided into two types. The first type is the static harmonics, which are constant and not affected by the perturbations, while the other is the dynamic harmonics which are changed along with perturbations. As for the static harmonics, the analytical methods have been well developed based on the double Fourier analysis [25]. However, the analysis of dynamic harmonics, which may have a significant influence on system dynamic performance and stability, are usually overlooked [22].

To fully capture the characteristics of dynamic harmonics, a small-signal perturbation is intentionally injected into the PWM reference waveform under $\alpha\beta$ frame, as shown in Fig. 2. Then by calculating the spectra of inverter output voltage analytically, the frequency response of the digital sinusoidal PWM modulator can be derived at both the perturbation frequency and sideband frequency based on the harmonic balance principle [26].

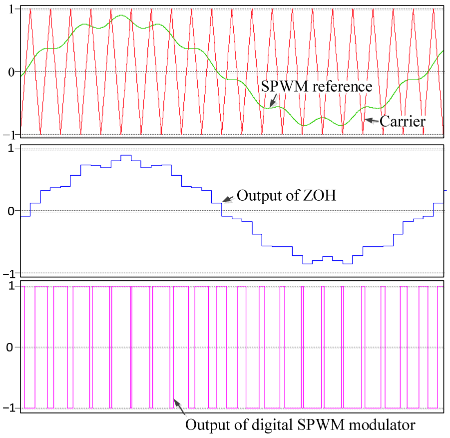

Fig. 1 Outputs of ZOH and the digital sinusoidal PWM modulator

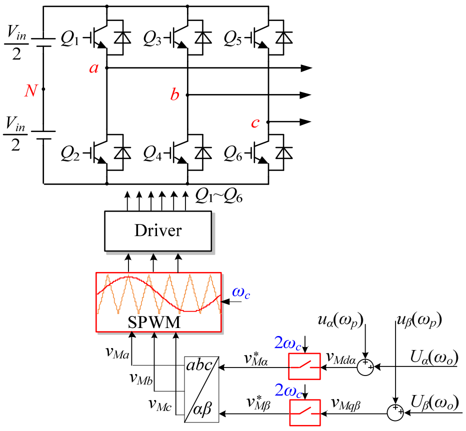

Fig. 2 Digital sinusoidal PWM modulator with small-signal perturbation

To simplify the analysis, all the variables are transferred to the $\alpha\beta$ frame and represented by the complex space vector. Thus, the three-phase system can be represented by single-phase system, provided that the three-phase components are balanced. As shown in Fig. 2, the angular frequency of the carrier waveform is ω_c, and the sampling frequency is ω_s. In this work, the double update of the duty cycle is adopted, i.e. the digital control system is sampled and updated twice for each switching cycle, $\omega_s = 2\omega_c$ [22]. A small-signal perturbation component $u_{\alpha\beta}$ at the frequency ω_p is intentionally added to the fundamental wave $U_{\alpha\beta}$. The complex vectors of $u_{\alpha\beta}$ and $U_{\alpha\beta}$ in the frequency domain can be represented by:

$$\boldsymbol{u}_{\alpha\beta}(\omega)=u_\alpha(\omega)+ju_\beta(\omega)=M_p 2\pi\cdot e^{j\theta_p}\cdot\delta\left(\omega-\omega_p\right). \tag{2}$$

$$\boldsymbol{U}_{\alpha\beta}(\omega)=U_\alpha(\omega)+jU_\beta(\omega)=M_0 2\pi\cdot e^{j\theta_0}\cdot\delta\left(\omega-\omega_0\right). \tag{3}$$

where M_p and M_0 are the modulation ratios of $u_{\alpha\beta}$ and $U_{\alpha\beta}$, respectively; θ_p and θ_0 are initial phase angle of $u_{\alpha\beta}$ and $U_{\alpha\beta}$, respectively. Under small-signal assumption, we have $M_p \ll M_0$.

Using one-dimensional spectral analysis method proposed in [27], the harmonic spectrum of inverter output voltages in the $\alpha\beta$ frame can be derived as (4)

$$\begin{aligned}&\boldsymbol{v}_{\boldsymbol{inv\_\alpha\beta}}(\omega)=u_{inv\_\alpha}(\omega)+ju_{inv\_\beta}(\omega)\\&=\sum_{m=-\infty}^{\infty}\sum_{n_0=-\infty}^{\infty}\sum_{n_p=-\infty}^{\infty}\left\{\begin{aligned}&\left(\begin{aligned}&\frac{2}{3}\left(1-2\cos\left(\frac{2n_0+2n_p+1}{3}\pi\right)\right)\cdot\frac{4}{m+n_0\frac{\omega_0}{\omega_c}+n_p\frac{\omega_p}{\omega_c}}\sin\left(\left(m+n_0+n_p\right)\frac{\pi}{2}\right)\\&\cdot J_{n_0}\left(\frac{\pi}{2}\left(m+n_0\frac{\omega_0}{\omega_c}+n_p\frac{\omega_p}{\omega_c}\right)M_0\right)\cdot J_{n_p}\left(\frac{\pi}{2}\left(m+n_0\frac{\omega_0}{\omega_c}+n_p\frac{\omega_p}{\omega_c}\right)M_p\right)\cdot e^{j\left(n_0\theta_0+n_p\theta_p+m\theta_c\right)}\cdot\delta\left(\omega-m\omega_c-n_0\omega_0-n_p\omega_p\right)\end{aligned}\right)\\+&\left(\begin{aligned}&\frac{2}{3}\left(1-2\cos\left(\frac{2n_0+2n_p-1}{3}\pi\right)\right)\cdot\frac{4}{m+n_0\frac{\omega_0}{\omega_c}+n_p\frac{\omega_p}{\omega_c}}\sin\left(\left(m+n_0+n_p\right)\frac{\pi}{2}\right)\\&\cdot J_{n_0}\left(\frac{\pi}{2}\left(m+n_0\frac{\omega_0}{\omega_c}+n_p\frac{\omega_p}{\omega_c}\right)M_0\right)\cdot J_{n_p}\left(\frac{\pi}{2}\left(m+n_0\frac{\omega_0}{\omega_c}+n_p\frac{\omega_p}{\omega_c}\right)M_p\right)\cdot e^{-j\left(n_0\theta_0+n_p\theta_p+m\theta_c\right)}\cdot\delta\left(\omega+m\omega_c+n_0\omega_0+n_p\omega_p\right)\end{aligned}\right)\end{aligned}\right\}.\qquad(4)\end{aligned}$$

where θ_c, is the initial phase angle of the carrier, and m, n_0 and n_p are the index variables of the carrier, fundamental wave and small-signal perturbation, respectively. J_n is the n order of first kind Bessel function, which is expressed as

$$J_n(x)=\frac{1}{2\pi}\int_0^{2\pi}\cos(n\tau-x\sin\tau)d\tau \qquad (5)$$

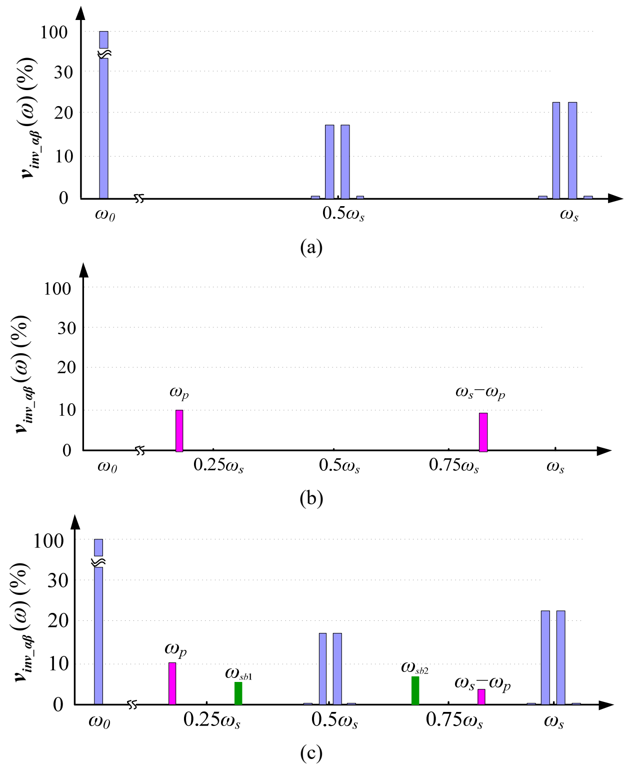

Fig. 3 Harmonic spectra of the inverter output voltage with PWM reference containing (a) only fundamental wave, (b) only small-signal perturbation, (c) both the fundamental wave and small signal perturbation.

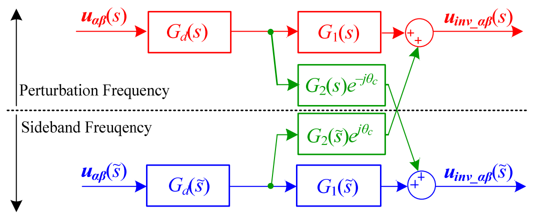

Fig. 4 Multi-frequency model for the digital sinusoidal PWM modulator

According to the Fourier analysis given in (4), the harmonic spectra of the inverter output voltage in the three different cases are shown in Fig. 3. First, when the PWM reference contains only the sinusoidal fundamental waveform, as shown in Fig. 3(a), the dominant harmonics are around $0.5\omega_s$ and ω_s, which are static harmonics. Secondly, when the PWM reference contains only the small-signal perturbation ω_p, as shown in Fig. 3(b), the resulting sideband harmonic is at the frequency $\omega_s-\omega_p$, which is the dynamic harmonic. Lastly, when the PWM reference contains both the sinusoidal fundamental wave and the small-signal perturbation, as shown in Fig. 3(c), the static harmonics are the same with that in Fig. 3(a). However, the dynamic harmonics are different from that in Fig. 3(b). New sideband harmonic components are generated at the relatively low-frequency range, of which the frequencies ω_{sb1} and ω_{sb2} are also affected by the phase sequence of the perturbation.

In this paper, it is assumed that the dynamic harmonic components beyond the Nyquist frequency $0.5\omega_s$ are well attenuated by the power filter and the anti-aliasing filter. Only the lowest sideband harmonic at ω_{sb1} is taken into account when modeling the digital sinusoidal PWM modulator.

According to (2) and (4), the relationship between the perturbation and the corresponding dominant sideband components is derived based on the harmonic balance principle, which is illustrated by the multi-frequency model shown in Fig. 4. The dynamics of two frequency components, i.e., the perturbation frequency component and the sideband frequency component, have been taken into consideration. As for the positive sequence perturbation, i.e., $\omega_p\geq0$, the dominant sideband component is $\omega_{sb1}=\omega_p+\omega_0-\omega_c$. If $s=j\omega_p$ is used as the Laplace variable at the perturbation frequency, $\tilde{s}=s+j\left(\omega_0-\omega_c\right)$ is thereby used as Laplace variable at the sideband frequency. As for the negative sequence perturbation, i.e., $\omega_p<0$, the dominated sideband component is $\omega_{sb1}=\omega_p+\omega_0+\omega_c$, so $\tilde{s}=s+j(\omega_0+\omega_c)$ is thereby used as Laplace variable of the sideband frequency.

In Fig. 4, $G_d(s)$ represents the delay caused by the computation and ZOH, which is given by

$$G_d(s)=e^{-1.5sT_s}. \qquad (6)$$

$G_1(s)$ is the transfer function of the sampler and modulator of the single frequency, which is expressed as:

$$G_1(s)=J_0\left(\frac{\pi}{2}\frac{|s|}{\omega_c}\mathrm{M}_0\right).\tag{7}$$

$G_2(s)$ is the transfer function denoting the dynamic coupling between the perturbation frequency and the sideband frequency components. Since the dominant side-band frequency is different for the positive-sequence and negative-sequence component of $u_{\alpha\beta}(\omega_p)$, the expression of $G_2(s)$ is also different depending on the sequence of $u_{\alpha\beta}(\omega_p)$, which is given by

$$G_2(s)=\begin{cases}-J_1\left(\frac{\pi}{2}\left(1-\frac{|s|+\omega_0}{\omega_c}\right)\mathrm{M}_0\right)\left(\omega_p\geq 0\right)\\ -J_1\left(\frac{\pi}{2}\left(1+\frac{-|s|+\omega_0}{\omega_c}\right)\mathrm{M}_0\right)\left(\omega_p<0\right)\end{cases}.\tag{8}$$

It is worth noting that this multi-frequency model can be readily transformed from the $\alpha\beta$-frame to the dq-frame, simply by replacing the Laplace variables s and $\tilde{s}$ with $s+j\omega_0$ and $\tilde{s}+j\omega_0$, respectively, according to the frequency translation between the $\alpha\beta$ frame and dq frame [5].

III. MULTI-FREQUENCY IMPEDANCE MODELING

To analyze the impact of asynchronous carriers on the stability of the paralleled inverters, the multi-frequency impedance model of the single grid-connected inverter will be firstly established, and then extended to the paralleled inverters.

A. Single Inverter

The control scheme of a three-phase grid-connected inverter with LCL filter is shown in Fig. 5, where v_{pcc_a}, v_{pcc_b}, and v_{pcc_c} are the three-phase grid voltages at the point of common coupling (PCC). In this paper, the inverter-side currents are controlled in the $\alpha\beta$ frame, and the capacitor voltage v_C is fed forward to actively damp resonance peak of the LCL filter. G_i is the current regulator, and G_v is the feedforward function.

The corresponding control block diagram is shown in Fig. 6, from which the control output admittance considering the sideband effect can be derived as:

$$\boldsymbol{Y_o}=\left[\boldsymbol{Y_{inv}}+\boldsymbol{Y_C}\right]\times\left[\boldsymbol{Y_{inv}}+\boldsymbol{Y_C}+\boldsymbol{Y_{L2}}\right]^{-1}\times\boldsymbol{Y_{L2}}.\tag{9}$$

where Y_C and Y_{L2} are the admittance matrices of capacitor C and inductor L_2, which are expressed as $\boldsymbol{Y_C}=\left[sC\ 0;\ 0\ \tilde{s}C\right]$, $\boldsymbol{Y_{L2}}=\left[1/sL_2\ \ 0;\ 0\ \ 1/\tilde{s}L_2\right]$, and Y_{inv} is the closed-loop admittance matrix of the L-inverter, which is expressed as (10) at the bottom of this page, where I is the identity matrix. Similarly, the gird impedance matrix is denoted by $\boldsymbol{Z_g}=\left[sL_g\ \ 0;\ 0\ \ 1/\tilde{s}L_g\right]$. As seen, the dynamic behavior of the single inverter is represented by the two-input-two-output impedance matrix, which contains both the perturbance frequency component and the sideband frequency component, as well as the coupling effect between them.

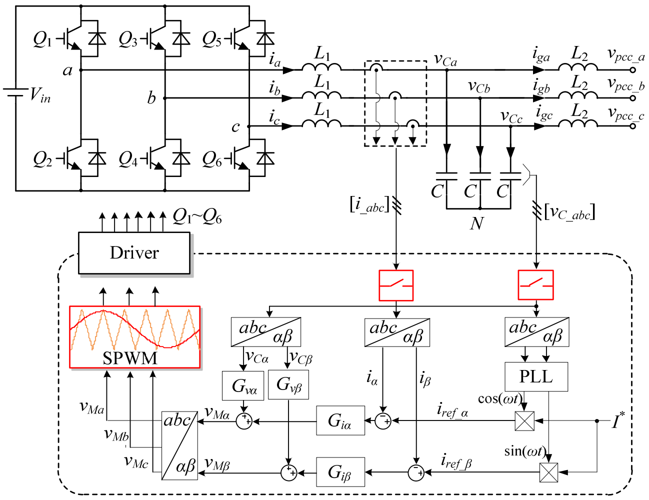

Fig. 5 Control scheme of the three-phase grid-connected inverter

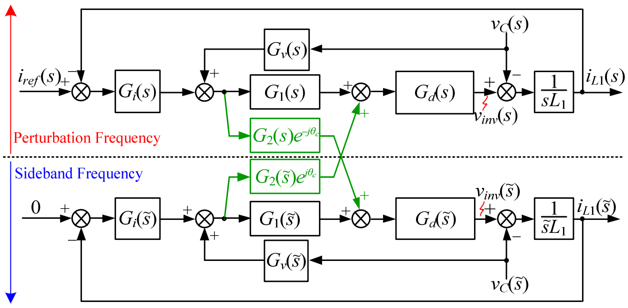

Fig. 6 Control block diagram of the three-phase grid-connected inverter

B. Paralleled Inverters

Based on the multi-frequency impedance model of the single inverter, the simplified circuit model of paralleled inverters is depicted by the Fig. 7, and the corresponding control block diagram is shown in Fig. 8. The dynamics of inverters are coupled with each other through the upstream grid impedance Z_g. Since the cross-coupling effect between the perturbation frequency component and the sideband frequency component can be depicted by the cross-coupling impedance term in the impedance matrix with the information of the phase angle of the carrier included, the dynamic interactions among the inverters with asynchronous carriers can be well depicted, which will be analyzed in detail in the next section.

$$\boldsymbol{Y_{inv}}=\left[\begin{bmatrix}\frac{1}{sL_1}&0\\0&\frac{1}{\tilde{s}L_1}\end{bmatrix}-\begin{bmatrix}\frac{G_d(s)}{sL_1}&0\\0&\frac{G_d(\tilde{s})}{\tilde{s}L_1}\end{bmatrix}\begin{bmatrix}G_1(s)&G_2(\tilde{s})e^{j\theta_c}\\G_2(s)e^{-j\theta_c}&G_1(\tilde{s})\end{bmatrix}\begin{bmatrix}G_v(s)&0\\0&G_v(\tilde{s})\end{bmatrix}\right]\times\left[\boldsymbol{I}+\begin{bmatrix}\frac{G_d(s)}{sL_1}&0\\0&\frac{G_d(\tilde{s})}{\tilde{s}L_1}\end{bmatrix}\begin{bmatrix}G_1(s)&G_2(\tilde{s})e^{j\theta_c}\\G_2(s)e^{-j\theta_c}&G_1(\tilde{s})\end{bmatrix}\begin{bmatrix}G_i(s)&0\\0&G_i(\tilde{s})\end{bmatrix}\right]^{-1}.\tag{10}$$

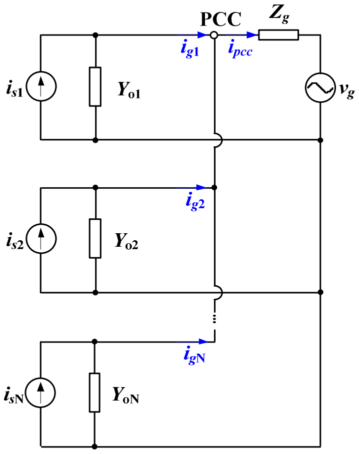

Fig.7 Simplified circuit model of paralleled inverters

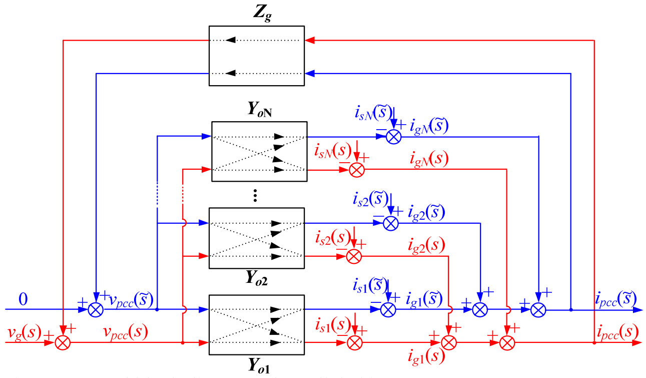

Fig.8 Control block diagram of paralleled inverters

IV. Stability Analysis and Experimental Verification

All the impedances/admittances are represented by two-input-two-output matrices, which can accurately model the dynamics of paralleled inverters with consideration of sideband components determined by angles of carriers. Therefore, the sideband harmonic instability caused by the asynchronous carriers can be revealed. According to Fig. 8, the return ratio for the grid current of k# inverter L_{igk} can be expressed by:

$$L_{igk} = \left[\sum_{\substack{i=1 \\ i\neq k}}^{N} Y_{oi} + Z_g^{-1} \right]^{-1} \times Y_{ok} \,. \tag{11}$$

By plotting the Bode diagram of the eigenvalues of the return ratio L_{igk}, the stability for the grid current of the k# inverter can be justified [28]. Due to the frequency coupling effect that described by the coupling terms of the inverter impedance matrix, stability problem can be aroused even if the system is designed both interactive and commonly stable. That is to say, even if the system is designed to be stable under both the stiff grid condition and the weak grid condition, the coupling effects between perturbation frequency domain and the sideband frequency domain can trigger additional stability frequency problem. This instability cannot be predicted by the averaged small signal model, which neglects the sideband components.

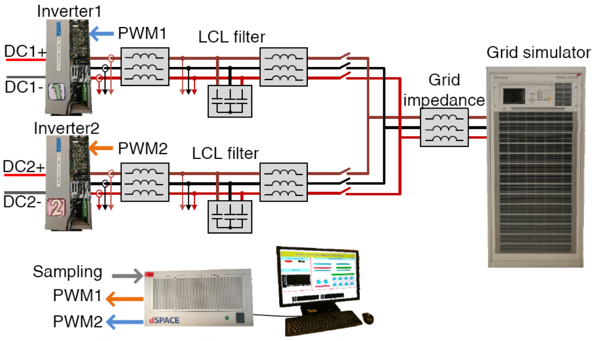

Fig. 9 Configuration of the experimental setup.

TABLE I

PARAMETERS OF GRID CONNECTED INVERTER

	Parameter	Values
V_{in}	Input dc-link voltage	600 V
V_g	Phase grid voltage, RMS	110 V
f_0	Fundamental frequency	50 Hz
f_{sw}	Switching frequency	6 kHz
f_s	Sampling frequency	12 kHz
L_1	Inverter-side inductor	1.5mH
C	Filter capacitor	5μF
L_2	Grid-side inductor	1.5mH
L_g	Grid impedance	1.5mH

The experimental setup is shown in Fig. 9, where the weak grid is realized by connecting the inductors with the grid simulator, and control algorithms of the two inverters are implemented in one dSPACE so that carrier angles of two inverters can be adjusted flexibly. The anti-aliasing filter is intentionally added to filter out the high-frequency sideband components beyond the Nyquist frequency. The circuit parameters are shown in Table I.

Fig. 10 (a) shows Bode diagrams of eigenvalues of L_{ig1} when the carriers of the inverters are synchronous, i.e., $\theta_{c1}=\theta_{c2}$. Since the coupling terms of the modulator $G_2(s)$ is different as for the negative sequence and positive sequence, both the negative-sequence and positive-sequence frequency responses of L_{ig1} are presented. As can be seen, the phase responses of all eigenvalues are limited within −180°~180°. Therefore, the system should be stable according to the Nyquist stability criterion. Fig. 10 (b) shows Bode diagrams of eigenvalues of L_{ig1} when inverter 1# is asynchronous with inverter 2#, i.e., $\theta_{c1}-\theta_{c2}$ =180°. As can be seen, the negative crosses are generated around −3.4kHz and −2.7kHz, which implies that the system is unstable and resonances are expected to be in the negative sequence.

Figs. 11 and 12 give the steady-state and dynamic experimental results, respectively. It is clear that the system is stable when all the inverters are synchronous, and the resonance between the inverters arises when the carriers of inverters are asynchronous. According to the FFT analysis, the resonance is mainly around 2.7kHz, while the resonance at the sideband frequency 3.4kHz is almost canceled due to phase-shift of the sideband component according to Fig. 3. So the experimental results confirm the effectiveness of

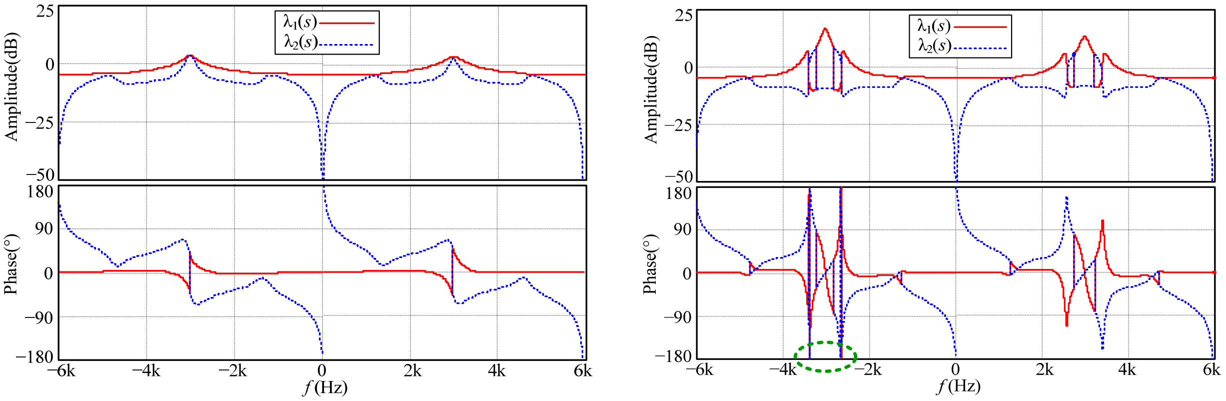

(a) (b)

Fig. 10 Bode diagram of eigenvalues under (a) synchronous condition (b) asynchronous condition

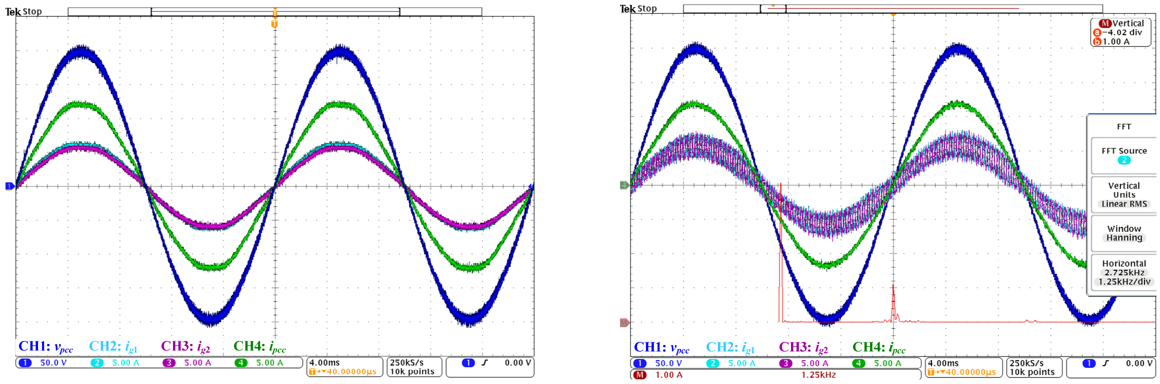

(a) (b)

Fig. 11 Steady-state waveforms when carriers are (a) synchronous, (b) asynchronous.

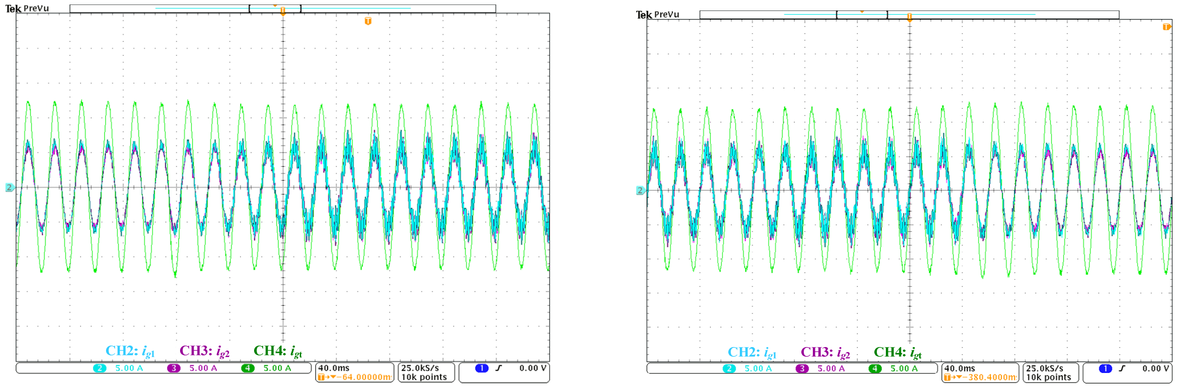

(a) (b)

Fig. 12 Dynamic waveforms when carriers are adjusted (a) from synchronous to asynchronous, (b) from asynchronous to synchronous.

developed multi-frequency impedance model and the theoretical analysis.

To eliminate the sideband harmonic instability, a straightforward way is to make all the inverter carriers synchronized. This can be realized by the global synchronization method [29] through communication channels, such as RS485, RS232, power line carrier, or optical fiber. When the communication channels are not available, it is desirable to eliminate the sideband harmonic instability by incorporating the damping control in each inverter. Compared with the traditional harmonic instability, it is more challenging to damp the sideband harmonic instability which usually occurs beyond the Nyquist frequency. Basically, the damping control can be classified into the active type and passive type. The active damping can mimic the behavior of the resistor through the control, which does not introduce additional power loss [15]. However, the damping performance of this method can be degraded by the digital control delay, especially in the high-frequency range. On the other hand, the passive damping can provide effective damping over the full frequency range by using a real resistor[30]. Nevertheless, it may result in considerable power losses. Therefore, the combined active and passive damping method could be the practical solution to address the sideband harmonic instability issue.

V. CONCLUSION

For the paralleled inverters with asynchronous carriers, the sideband harmonics, produced by the pulse width modulation, tend to be different from one inverter to another, and can trigger the harmonic resonance and instability among the paralleled inverters. By investigating the harmonic spectrum of the digital sinusoidal PWM modulator, the multi-frequency impedance model is established to accurately describe the output behavior of inverter at the PCC point including the sideband components. The dynamic effect of the asynchronous carriers can thus be analyzed, and the frequency and phase sequence of the resonances can be predicted. The experimental results from two-paralleled inverters confirm the effectiveness of the developed model and corresponding stability analysis.

VI. REFERENCES

[1] F. Blaabjerg, R. Teodorescu, M. Liserre, and A. V. Timbus, “Overview of control and grid synchronization for distributed power generation systems,” *IEEE Trans. Ind. Electron.*, vol. 53, no. 5, pp. 1398−1409, Oct., 2006.

[2] X. Wang; F. Blaabjerg, W. Wu, “Modeling and analysis of harmonic stability in an AC power-electronics-based power system,” *IEEE Trans. Power Electron.*, vol. 29, no. 12, pp. 6421-6432, Dec., 2014.

[3] T. Messo, J. Jokipii, A. Makinen, and T. Suntio, “Modeling the grid synchronization induced negative-resistor-like behavior in the output impedance of a three-phase photovoltaic inverter,” in *Proc. IEEE Fourth Intl. Symp. Power Electron. for Distributed Generations System*, 2013, pp. 1–8.

[4] W. Bo, D. Dong, D. Boroyevich, R. Burgos, P. Mattavelli, and S. Zhiyu, "Impedance-based analysis of grid-synchronization stability for three-phase paralleled converters," *IEEE Trans. Power Electro*n., vol. 31, no.1, pp. 26–38, Jan., 2016.

[5] X. Wang, L. Harnefors, and F. Blaabjerg, “A unified impedance model of grid-connected voltage-source converters,” *IEEE Trans. Power Electron.,* in press.

[6] Y. Huang, X. Yuan, J. Hu, P. Zhou, “Modeling of VSC connected to weak grid for stability analysis of DC-Link voltage control,” *IEEE J. Emerg. Sel. Topics Power Electron.,* vol. 3, no. 4, pp. 1193–1204, Apr., 2015.

[7] Y. Huang, X. Yuan, J. Hu “Effect of reactive power control on stability of DC-link voltage control in VSC connected to weak grid” in *Proc. IEEE PES General Meeting*, 2014, pp.1–5.

[8] Y. Hao, X. Yuan, and J. Hu “Modeling of grid-connected VSCs for power system small-signal stability analysis in DC-Link voltage control timescale” *IEEE Trans. Power Electron.*, DOI: 10.1109/TPWRS.2017.2653939.

[9] X. Wang, F. Blaabjerg, Z. Chen, and W. Wu, “Resonance analysis in parallel voltage-controlled distributed generation inverters,” in *Proc. Annu. IEEE Appl. Power Electron. Conf. and Expo.*, 2013, pp. 2977–2983.

[10] S. Zhang, S. Jiang, X. Lu, B. Ge, and F. Z. Peng, “Resonance issues and damping techniques for grid-connected inverters with long transmission cable,” *IEEE Trans. Power Electron.*, vol. 29, no. 1, pp. 110–120, Jan., 2014.

[11] M. Lu, X. Wang, P. C. Loh, F. Blaabjerg, “Resonance interaction of multi-parallel grid-connected inverters with LCL filter,” *IEEE Trans. Power Electron.*, vol. 32, no. 2, pp. 894−899, Feb., 2017.

[12] L. H. Kocewiak, J. Hjerrild, and C. L. Bak, “Wind turbine converter control interaction with complex wind farm systems,” *IET Renewable Power Generation*, vol. 7, no. 4, pp. 380–389, Jul., 2013.

[13] H. M. Roudsari, A. Jalilian, and S. Jamali, “Resonance assessment in electrified railway systems using comprehensive model of train and overhead catenary system,” in *Proc. IEEE Int. Conf. Ind. Technol.*, Mar., 2015, pp. 1142–1148.

[14] J. Sun, “Impedance-based stability criterion for grid-connected inverters,” *IEEE Trans. Power Electron.*, vol. 26, no. 11, pp. 3075–3078, Nov., 2011.

[15] L. Harnefors, L. Zhang, andM. Bongiorno, “Frequency-domain passivity based current controller design,” *IET Power Electron.*, vol. 1, no. 4, pp. 455–465, Dec., 2008.

[16] D. Yang, X. Ruan, and H. Wu, “Impedance shaping of the grid-connected inverter with LCL filter to improve its adaptability to the weak grid condition,” IEEE Trans. Power Electron., vol. 29, no. 11, pp. 5795–5805, Nov., 2014.

[17] L. Harnefors, M. Bongiorno, and S. Lundberg, “Input-admittance calculation and shaping for controlled voltage-source converters,” *IEEE Trans. Ind. Electron.*, vol. 54, no. 6, pp. 3323–3334, Dec., 2007.

[18] J. Agorreta, M. Borrega, J. Lopez, and L. Marroyo, “Modeling and control of N-paralleled grid-connected inverters with LCL filters coupled due to grid impedance in PV plants, ” *IEEE Trans. Power Electron*., vol. 26, no. 3, pp. 770-1194, Mar., 2011.

[19] Y. Tang, W. Yao, P. Loh, and F. Blaabjerg, “Design of LCL-filters with LCL resonance frequencies beyond the Nyquist frequency for grid-connected converters,” *IEEE J. Emerg. Sel. Topics Power Electron*., vol. 4, no. 1, pp. 3–14, Mar., 2015.

[20] W. Wu, Y. He, and F. Blaabjerg, “An LLCL power filter for single-phase grid-tied inverter,” *IEEE Trans. Power Electron*., vol. 27, no. 2, pp. 782–789, Jan., 2012.

[21] J. Xu, J. Yang, J. Ye, Z. Zhang, and A. Shen, “An LTCL filter for three-phase grid-connected converters,” *IEEE Trans. Power Electron*., vol. 29, no. 8, pp. 4322–4338, Aug., 2014.

[22] C. Yu, X. Zhang, F. Liu, et al, “Modeling and resonance analysis of multi-parallel inverters system under asynchronous carriers conditions,” *IEEE Trans. Power Electron.*, vol. 32, no. 4, pp. 3192–3205, Aug., 2017.

[23] X. Yue, D. Boroyevich, R. Burgos, and F. Zhuo, “A frequency domain model for beat frequency oscillation analysis in microgrid,” in *Proc. IEEE ECCE Europe*, 2016, pp. 1−10.

[24] L. Harnefors, R. Finger, X. Wang, H. Bai, and F. Blaabjerg, “VSC input-admittance modeling and analysis above the Nyquist frequency for passivity-based stability assessment,” *IEEE Trans. Ind. Electron.,* in press.

[25] D. Holmes and T. Lipo, *Pulse Width Modulation for Power Converters (Principles and Practice)* (IEEE Press Series on Power Engineering). Hoboken, NJ, USA: Wiley 2003.

[26] J. Sun, Z. Bing, and K. J. Karimi, “Input impedance modeling of multipulse rectifiers by harmonic linearization,” *IEEE Trans. Power Electron*., vol. 24, no. 12, pp. 2812–2820, Dec., 2009.

[27] H. Mouton, B. McGrath, D. G. Holmes, R. H. Wilkinson, “One-dimensional spectral analysis of complex PWM waveforms using superposition,” *IEEE Trans. Power Electron*., vol. 29, no. 12, pp. 6762-6778, Dec., 2014.

[28] A. G. J. MacFarlane and I. Postlethwaite, “The generalized Nyquist stability criterion and multivariable root loci,” *Int. J. Control*, vol. 25, no. 1, pp. 81-127, Feb., 1977.

[29] T. Xu, F. Gao, “Global synchronous pulse width modulation of distributed inverters,” *IEEE Trans. Power Electron*., vol. 31, no. 9, pp. 6237-6253, Sep., 2016.

[30] X. Wang, R. Beres, F. Blaabjerg, and P. C. Loh, “Passivity-based design of passive damping for LCL-filtered voltage source converters,” in *Proc. IEEE Energy Convers. Congr. Expo. (ECCE)*, pp. 3718–3725, 2015.